nature astronomy

ARTICLES

https://doi.org/10.1038/s41550-020-1023-5

Check for updates

An extremely powerful long-lived superluminal ejection from the black hole MAXI J1820+070

J. S. Bright[1]✉, R. P. Fender[1,2], S. E. Motta[1], D. R. A. Williams[1], J. Moldon[3,4], R. M. Plotkin[5,6], J. C. A. Miller-Jones[6], I. Heywood[1,7,8], E. Tremou[9], R. Beswick[4], G. R. Sivakoff[10], S. Corbel[9,11], D. A. H. Buckley[12], J. Homan[13,14,15], E. Gallo[16], A. J. Tetarenko[17], T. D. Russell[18], D. A. Green[19], D. Titterington[19], P. A. Woudt[2,20], R. P. Armstrong[1,2,8], P. J. Groot[2,12,21], A. Horesh[22], A. J. van der Horst[23,24], E. G. Körding[21], V. A. McBride[2,12,25], A. Rowlinson[18,26] and R. A. M. J. Wijers[18]

Black holes in binary systems execute patterns of outburst activity where two characteristic X-ray states are associated with different behaviours observed at radio wavelengths. The hard state is associated with radio emission indicative of a continuously replenished, collimated, relativistic jet, whereas the soft state is rarely associated with radio emission, and never continuously, implying the absence of a quasi-steady jet. Here we report radio observations of the black hole transient MAXI J1820+070 during its 2018 outburst. As the black hole transitioned from the hard to soft state, we observed an isolated radio flare, which, using high-angular-resolution radio observations, we connect with the launch of bipolar relativistic ejecta. This flare occurs as the radio emission of the core jet is suppressed by a factor of over 800. We monitor the evolution of the ejecta over 200 days and to a maximum separation of 10″, during which period it remains detectable due to in situ particle acceleration. Using simultaneous radio observations sensitive to different angular scales, we calculate an accurate estimate of energy content of the approaching ejection. This energy estimate is far larger than that derived from the state transition radio flare, suggesting a systematic underestimate of jet energetics.

Black hole X-ray binary (BHXRB) systems consist of a stellar-mass black hole accreting material via Roche lobe overflow from a main-sequence companion star. X-ray observations of such systems, which probe their accretion flow, have revealed the existence of two primary accretion states, termed hard and soft[1,2]. In the hard state, the X-ray spectrum is non-thermal, and thought to be dominated by emission from an inner accretion disk corona. In the soft state, coronal emission is suppressed, and the X-ray spectrum is well described by thermal emission from the accretion disk itself. Contemporaneous radio observations, which probe the jets, show that the accretion state of a BHXRB system determines the form of the outflows it produces[1–5]. During the hard state, radio emission is from a flat-spectrum, collimated, compact (Solar System scale) jet[6,7], which is quenched in the soft state[8–11]. The most dramatic outburst behaviour occurs as sources transition from the hard to the soft accretion state. During the transition, as the core jet quenches, systems exhibit short-timescale (of the order hours) radio flaring superposed on the decaying core jet flux[1]. These flares have been associated with the ejection of discrete (apparently no longer connected spatially to the black hole) knots of material, which can be observed to move (sometimes apparently superluminally) away from the black hole, reaching separations tens of thousands times farther than that of the core jet[12]. The mechanism(s) causing the launch of these ejections, as well as the radio flaring, are not well understood. Jets and ejections represent two of the primary channels through which galactic black holes return matter and energy into their surroundings and studying them is key to understanding feedback processes and their effects on the environment from black holes over a range of mass scales.

MAXI J1820+070/ASASSN-18ey[13–16] (hereafter, J1820) was discovered at optical wavelengths by the All-Sky Automated Survey for SuperNovae (ASAS-SN[17]) project on 7 March 2018 (modified Julian date (MJD) 58184), and around 6 d later in X-rays by the Monitor of All-sky X-ray Image (MAXI[14]). Soon after, it was classified as

[1]Astrophysics, Department of Physics, University of Oxford, Oxford, UK. [2]Department of Astronomy, University of Cape Town, Rondenbosch, South Africa. [3]Instituto de Astrofísica de Andalucía (IAA, CSIC), Glorieta de las Astronomía, Granada, Spain. [4]Jodrell Bank Centre for Astrophysics, The University of Manchester, Manchester, UK. [5]Department of Physics, University of Nevada, Reno, NV, USA. [6]International Centre for Radio Astronomy Research, Curtin University, Perth, Western Australia, Australia. [7]Department of Physics and Electronics, Rhodes University, Grahamstown, South Africa. [8]South African Radio Astronomy Observatory (SARAO), Cape Town, South Africa. [9]AIM/CEA Paris-Saclay, Universitè Paris Diderot, CNRS, Gif-sur-Yvette, France. [10]Department of Physics, University of Alberta, Edmonton, Alberta, Canada. [11]Station de Radioastronomie de Nançay, Observatoire de Paris, PSL Research University, CNRS, Université d'Orléans, Nançay, France. [12]South African Astronomical Observatory, Cape Town, South Africa. [13]Eurika Scientific, Inc., Oakland, CA, USA. [14]SRON, Netherlands Institute for Space Research, Utrecht, The Netherlands. [15]MIT Kavli Institute for Astrophysics and Space Research, Cambridge, MA, USA. [16]Department of Astronomy, University of Michigan, Ann Arbor, MI, USA. [17]East Asian Observatory, Hilo, HI, USA. [18]Anton Pannekoek Institute, University of Amsterdam, Amsterdam, The Netherlands. [19]Astrophysics Group, Cavendish Laboratory, Cambridge, UK. [20]Inter-University Institute of Data Intensive Astronomy, Department of Astronomy, University of Cape Town, Cape Town, South Africa. [21]Department of Astrophysics/IMAPP, Radboud University Nijmegen, Nijmegen, The Netherlands. [22]Racah Institute of Physics, The Hebrew University of Jerusalem, Jerusalem, Israel. [23]Department of Physics, the George Washington University, Washington DC, USA. [24]Astronomy, Physics and Statistics Institute of Sciences (APSIS), Washington DC, USA. [25]IAU Office of Astronomy for Development, Cape Town, South Africa. [26]Netherlands Institute for Radio Astronomy (ASTRON), Dwingeloo, The Netherlands. ✉e-mail: joe.bright@physics.ox.ac.uk

a candidate BHXRB by the Neutron Star Interior Composition Explorer (NICER) on the basis of its timing properties[15] (and later dynamically confirmed from its mass function[16]). The Neil Gehrels Swift Observatory (Swift) Burst Alert Telescope (BAT) triggered on J1820 on MJD 58189[18], prompting rapid robotic follow-up[19] with the Arcminute Microkelvin Imager Large Array (AMI-LA) only 90 min later, the earliest radio detection of the outburst of a new BHXRB ever reported. The relatively close proximity[20] ($3.8^{+2.9}_{-1.2}$ kpc) and brightness of J1820 allowed for extremely good coverage of the outburst across the electromagnetic spectrum[13,21–25].

Results

Throughout its outburst, we monitored J1820 intensively with a range of radio telescopes: the AMI-LA, Multi-Element Radio Linked Interferometer Network (eMERLIN), Meer Karoo Array Telescope (MeerKAT), the Karl G. Jansky Very Large Array (VLA) and the Very Long Baseline Array (VLBA; ordered in terms of time spent on source; see Methods for the details of our observations) as well as at X-ray wavelengths with Swift. In Fig. 1, we present a subset of our over 200 d of 15.5 GHz radio monitoring as a function of X-ray luminosity, selecting only (quasi-)simultaneous observations. This radio–X-ray plane is typically used to study the nonlinear correlation between radio and X-ray fluxes from black holes in the hard state, from which radio emission is always detected, revealing the connection between accretion rate and jet power. Sources in the soft state, which corresponds to dramatically different accretion properties with respect to the hard state (Supplementary Information), are rarely detected in the radio band and consequently are not usually shown on the diagram. Our (quasi-)simultaneous radio and X-ray coverage includes the hard states at the start and the end of the outburst (before and after MJD 58303.5 and 58393, respectively), the entirety of the soft state (between MJD 58310.7 and 58380) and the intermediate states, where the relative X-ray emission contribution of the disk and corona are evolving quickly and the core radio jet is quenching or restarting (MJD 58303.5 to 58310.7, and MJD 58380 to 58393, respectively)[22]. During the decay phase (where the radio flux from the quenching core jet is dropping) after the initial hard state (that is, during the first intermediate state), we observe a ‘flare’ event, characterized by a short timescale rise and decay (~12 h in total) of the radio emission from J1820 (Extended Data Fig. 1). These events are thought to be caused not by the compact core jet, but instead by discrete relativistic ejections[26]. As expected, J1820 is detected throughout the hard state, as well as during the decay and rise (where the compact jet is now switching back on) phases before and after the soft state, respectively. The radio–X-ray correlation indicates that the source is ‘radio loud’ in the sense that it lies on the higher track in the plane, similarly to the archetypal source GX 339−4[27].

Remarkably, however, J1820 is also detected continuously, at a lower level, in 56 observations throughout its 80 d soft state (which are also demonstrated as a function of X-ray luminosity in Fig. 1). In the most comprehensive previous ensemble study of radio observations of the BHXRB soft state[26], it was demonstrated that for all but one source (XTE J1748−288[28]), there is either no radio emission, or only transient emission, during the soft state, and for that one exception the nature of the emission is very poorly determined. Since then, only one source, MAXI J1535−571, has shown such long-lived soft-state emission[11]. We show in Fig. 1 the previous deepest limits on radio emission in the soft state from other BHXRBs. On the basis of the AMI-LA radio-flux-density monitoring alone, the nature of the soft-state radio emission from J1820 is unclear. Without high-resolution radio images, the continued soft-state emission could, in principle, be interpreted as evidence for a causal connection between the accretion flow and radio emission, that is, ongoing core jet production in the soft state. A radio image with the VLBA (Extended Data Fig. 2), at 15 GHz, ~3 d into the intermediate state as J1820 transitioned from the hard to soft state reveals, however, that the core is not detected to a 3σ flux density limit of ~420 μJy beam^{-1}, and that there are components that can be associated with relativistic ejections both approaching and receding from the Earth. Images with eMERLIN (Fig. 2) over the following ~3 weeks show the approaching component moving away from the black hole. Further radio images with the eMERLIN, MeerKAT and VLA radio telescopes (Fig. 3), when J1820 had returned to the hard X-ray state, reveal that the approaching jet is still detected over 140 d after J1820 transitioned to the soft state. At later times, a receding ejection is resolved with MeerKAT and the VLA, which we observe up to 175 d after the start of the soft state. A comparison between the time evolution of the (frequency scaled) flux density from the resolved approaching ejection and the (unresolved) flux density measured by the AMI-LA during the soft state reveals that all of the radio emission can be attributed to this ejection (Figs. 3 and 4). The flux density from the approaching ejection shows multiple decay rates. After a short rise, the flux density decays with a timescale (e-folding time) of ~6 d. However, after ~10 d, it re-brightens and undergoes a much slower decay with a timescale of ~50 d, transitioning ~60 d later to a faster decay rate with an ~20 d timescale (Supplementary Information and Extended Data Fig. 4).

When fitting for the proper motion (angular velocity across the sky) of the approaching ($\mu_{\rm app}$) and receding ($\mu_{\rm rec}$) ejection components, we consider both a ballistic and constant deceleration model, finding linear proper motions of $\mu_{\rm app} = 77 \pm 1$ mas d^{-1} and $\mu_{\rm rec} = 33 \pm 1$ mas d^{-1}, and initial velocities of $\mu_{\rm app} = 101 \pm 3$ mas d^{-1} and $\mu_{\rm rec} = 58 \pm 6$ mas d^{-1} for a constant deceleration (Extended

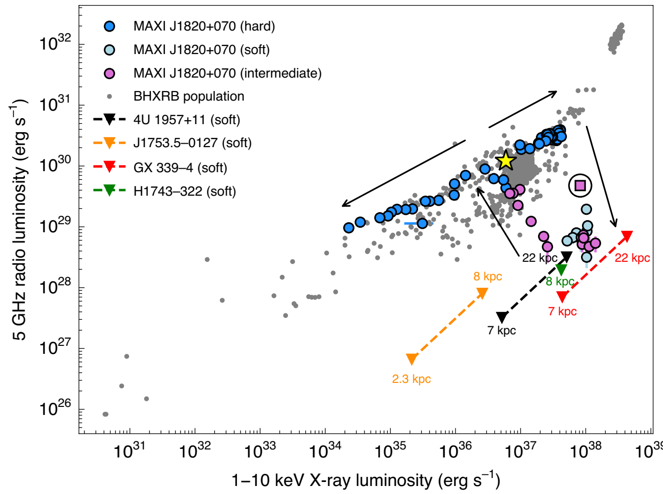

Fig. 1 | The radio–X-ray correlation for the BHXRB population and J1820. Radio luminosity as a function of X-ray luminosity for J1820, based on our monitoring at 15.5 GHz with the AMI-LA radio telescope (scaled to 5 GHz assuming a flat spectrum) and X-ray observations from the Swift XRT. The data for J1820 in the hard, soft and intermediate states are shown by dark blue, light blue and purple circles, respectively. For the majority of data points, the error bars are too small to be seen. The yellow star marks our first simultaneous radio/X-ray observation of J1820 (3.2 d after our first radio observation) and the black arrows show schematically the time evolution of the outburst. We only use X-ray observations within 8 h of our radio observations, with the exception of the purple square circumscribed with a circle. In this case, the observations were taken ~14 h apart. Error bars on data points indicate 1σ uncertainties. Data from the literature on other black hole systems are indicated by grey dots[54]. We mark upper limits for core soft-state emission from the XRB systems 4U1957+11, J1753.5−0127, GX 339−4 and H1743−322[8–10,55] for a range of possible distances. We do not include radio observations taken during the state transition flare. We use a distance of 3.1 kpc when calculating the luminosities[31].

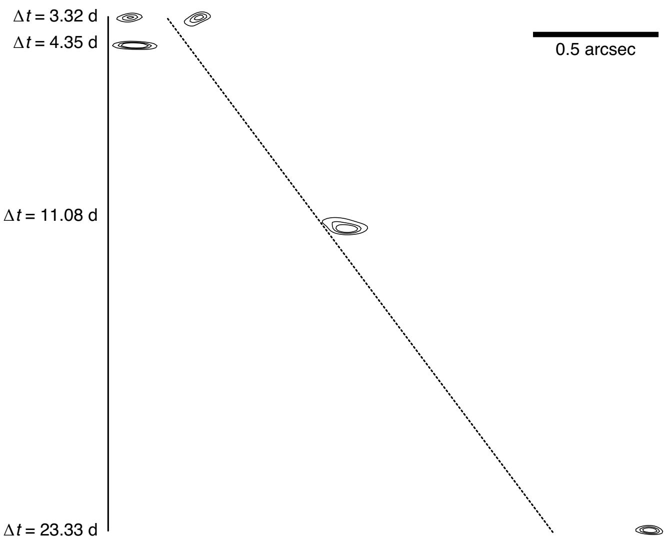

Fig. 2 | High-angular-resolution radio observations of J1820 made with eMERLIN. eMERLIN observations of J1820 show a jet component distinct from the black hole position. The beam sizes, chronologically, are 99.2 mas × 30.3 mas, 127.5 mas × 27.5 mas, 106.6 mas × 32.2 mas and 130.5 mas × 26.8 mas. All images have been rotated ~65° anticlockwise. Contours mark (105, 150, 60, 125) μJy beam^{-1} × log(n) for n = 4, 5, 6, where the pre-factor corresponds to the images chronologically. The black vertical solid line marks the position of the core, determined from a hard-state observation made with eMERLIN. The black dashed line shows the best-fit ballistic trajectory of the (approaching) ejection, with the fit constrained by all observations presented in Supplementary Table 1. Δt is the time in days since the start of a radio flare that occurred during the hard-to-soft-state transition ($\Delta t = 0$ at MJD 58305.68), and is shown to the left of each observation. All observations have the same angular scale, and a scale bar is shown in the top right of the figure. Details on the data reduction procedure are presented in Methods, and flux densities are presented in Supplementary Table 2.

Data Fig. 3). These are among the highest proper motions ever measured from an astronomical object outside of the Solar System. Our linear proper motion model corresponds to apparent transverse velocities of at least 1.7 c and 0.7 c (for the approaching and receding components, respectively, where c is the speed of light) at a distance of 3.8 kpc. J1820, therefore, becomes one of a small number of black hole binaries to have produced jets with apparent superluminal mot ion[11,12,29,30]. The launch date for both models is consistent with MJD 58306, coinciding with the radio flare observed with the AMI-LA during the intermediate state, as the source moved from the hard to the soft state. The proper motion of each ejection can be independently related to its velocity, ejection angle to the observer's line of sight, and the distance to the source from the observer. From a combination of the approaching and receding proper motions (from the linear fit), we can calculate the product $\beta \cos\theta = 0.40 \pm 0.02$ (where β is the ejection's velocity in units of c, and θ is the jet inclination angle), a quantity that is independent of distance and assumes symmetric ejections with the same speeds[12]. From this, we constrain a maximum angle to the line of sight of $66° \pm 1°$ (for $\beta = 1$). We can also calculate a maximum distance to the source of 3.5 ± 0.2 kpc. This corresponds to the distance beyond which a more extreme angle to the line of sight than our calculated maximum angle would be required to explain the observed proper motions. For the constant deceleration model, we find a maximum angle to the line of sight of $74° \pm 2°$ and a maximum distance of 2.3 ± 0.6 kpc, respectively. However, a measured radio parallax distance to J1820 of 3.1 ± 0.3 kpc rules out the deceleration model[31]. The uncertainty in distance, combined with a highly relativistic jet, means that we can only place a lower limit on its bulk Lorentz factor of $\Gamma > 1.7$ (the apparent velocity, corresponding to $v > 0.8\,c$)[32].

On MJD 58396 ($\Delta t = 91.02$ d) and 58398 ($\Delta t = 93.01$ d), we observed J1820 with MeerKAT and eMERLIN, respectively, at very similar frequencies (1.28 GHz and 1.51 GHz). These telescopes probe very different angular scales, with synthesiszed beams of 7.9″ × 5.4″ and 0.31″ × 0.2″, respectively. In both observations, the approaching jet component is detected. The flux density measured by MeerKAT is around 2 mJy, approximately 85% of which is resolved out at the angular scales probed by eMERLIN (which, due to its longer baselines, is not sensitive to structure on the angular scales probed by MeerKAT and thus recovers only 0.3 mJy). Although these observations were not taken strictly simultaneously, the time difference between the two observations is probably not enough to account for this large discrepancy given the observed decay rate (Supplementary Information). Taking the minimum angular size probed by each observation and the radio parallax distance allows us to set a range of sizes that the ~85% resolved out flux density (~1.7 mJy) is emitted from: between ~6.2×10^2 au and ~1.7×10^4 au. The emitting region size is the most important measurement for estimating the internal energy of a synchrotron-emitting plasma (which would be substantially underestimated by the integrated radiative power output over our observing campaign). Using our physical size constraints, we calculate[33] lower limits to the internal energy in the range 2.1×10^{41} erg $< E_f < 1.5 \times 10^{43}$ erg at the time of these near-simultaneous observations. This also allows us to constrain the equipartition magnetic field corresponding to this range of energies to be between 4.9×10^{-5} G and 8.3×10^{-4} G. Our derived lower limit to the minimum energy is orders of magnitude larger than the internal energy associated with the radio flare (E_i; thought to be a signature of the launch of transient ejections) observed during the hard-to-soft-state transition[34]. This flare had an associated minimum internal energy of $E_i \approx 2 \times 10^{37}$ erg. This estimate assumes that the flare is the result of the launch of an expanding plasmoid (synchrotron emitting plasma), with the peak caused by an optical depth transition from thick to thin[35–37]. A larger internal energy estimate can be derived from the peak flux density of the flare (~46 mJy) and its rise time (~6.7 h), giving $E_i = 2 \times 10^{39}$ erg, where we assume an expansion speed of 0.05 c (there is strong evidence[11,36,37] to suggest that these ejections expand much slower than c). However, this larger estimate for the flare's energetics is still two orders of magnitude below the estimate of the ejecta energetics.

Discussion

Persistent, slowly evolving radio emission from moving relativistic ejections has been observed in three XRB systems (XTE J1550−564, H1743−322 and MAXI J1535−571) previously. In XTE J1550−564, dynamic ejections were observed on small (<300 mas) angular scales following a radio flare[38]. These ejections then went 'dark', and were detected again over 2 yr later due to a re-brightening episode thought to be the result of an interaction with the wall of an interstellar medium (ISM) density cavity[39–41]. A similar explanation has been invoked to explain the large-scale jets in H1743−322[42]. In MAXI J1535−571, the approaching ejection was tracked for ~300 d, after being detected for the first time ~90 d after its inferred launch date[11]. The ejection was not resolved at an angular separation from the core of less than 4″, but was tracked out to over 15″. This allowed the launch time to be constrained to an ~5 d window, consistent with occurring just before a radio flaring event (although the start time of the flare is not well constrained). The flux density from the ejection decayed steadily, with re-brightening events possibly indicating internal shocks in the ejecta or interaction with ISM density enhancements. Our radio observations of J1820 track the entire evolution of the approaching ejecta, where we temporally

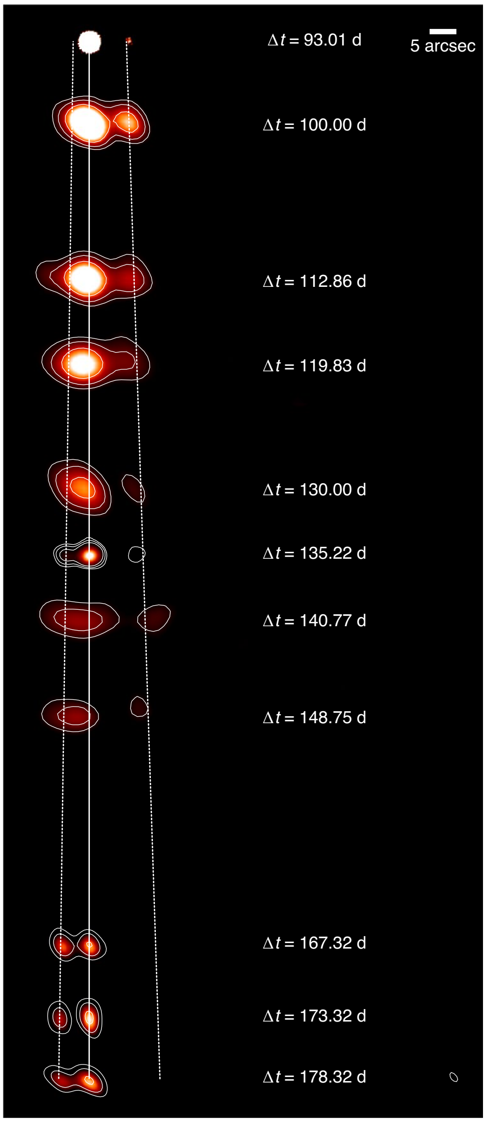

Fig. 3 | A subset of our resolved images of the core and ejections from J1820. A subset of images of J1820 from eMERLIN ($\Delta t = 93.01$ d) MeerKAT ($\Delta t = 100.00$, 112.86, 119.83, 130.00, 140.77 and 148.75 d) and the VLA ($\Delta t = 135.22$, 167.32, 173.32 and 178.32 d) where we resolve at least one ejecta from the core. All images have been rotated ~65° anticlockwise. Δt is the time in days since the start of the radio flare that occurred during the hard-to-soft-state transition ($\Delta t = 0$ at MJD 58305.68), and is shown to the right of each observation. All observations are shown with the same angular scale, and a scale bar is shown in the top right of the figure. For the MeerKAT observations, contours show 40 μJy beam$^{-1} \times (\sqrt{2})^n$ for $n = 4$, 6, 8 and the colour scale is linear between 0.1 and 1 mJy beam^{-1}. For the VLA observations, contours show 8 μJy beam$^{-1} \times (\sqrt{2})^n$ for $n = 4$, 6, 8, and the colour scale is linear between 0.05 and 0.15 mJy beam^{-1} for all but the first observation, which shares the same scale as the MeerKAT data. The colour scale for the eMERLIN observation is linear between 0.2 and 0.3 mJy beam^{-1}. The white vertical solid line marks the position of the core, determined from hard-state observations made with eMERLIN. The right and left dashed lines show the best fit ballistic trajectory of approaching and receding ejection components, respectively. These fits are constrained by the observations presented in Supplementary Table 1. Details on the data reduction procedure are presented in Methods.

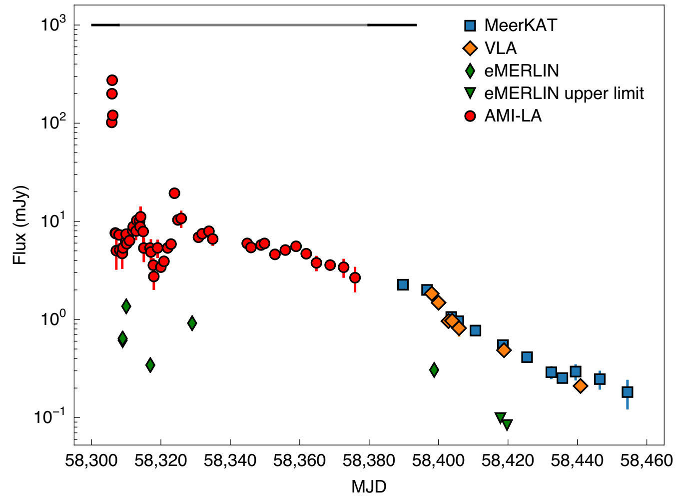

Fig. 4 | The radio flux density from the approaching radio ejecta over a 150 d period, starting near our inferred ejection time. Data taken at different frequencies have been scaled by a spectral index $\alpha = -0.7$ ($F_\nu = A\nu^\alpha$; appropriate for optically thin synchrotron emission from jet ejecta where F_ν is the flux density at the frequency ν, and A is a flux density scaling factor) to a common frequency of 1.28 GHz. We do not scale the upper limits. The MeerKAT, eMERLIN and VLA data are measurements of the approaching jet flux density from images in which it is clearly spatially resolved from the core. We do not include AMI-LA data after J1820 returned to the hard state (around MJD 58390) as the flux density was dominated by the re-brightened core after this time. The grey horizontal line marks the duration of the soft state, and the black lines the intermediate state. Error bars on data points indicate 1σ uncertainties.

resolve the transition from a short-timescale decay phase (more typical of the timescales associated with transient soft-state emission), a subsequent re-brightening, and then a long-timescale decay phase (see Supplementary Information for a discussion of the decay rates, and comparison with other sources). The most likely explanation for the slowly decaying flux density is that there is constant in situ particle acceleration as the jet decelerates via interactions with the nearby ISM[43]. In this scenario, by the time of our energetic analysis based on the resolved emission, all of the supplied energy, E_f, responsible for the observed radio emission would have come from this deceleration. The kinetic energy of the ejecta at a given moment is $\mathrm{KE} = (\Gamma - 1)E$, where E is the internal energy of the ejecta and Γ is the bulk Lorentz factor. We denote the initial and final (at the time of our measurement of E_f) internal energies and Lorentz factors by the subscripts (i,f). From the condition that deceleration has provided the observed energy, we have that $(\mathrm{KE})_i - (\mathrm{KE})_f \gtrsim E_f$ or, equivalently, $(\mathrm{KE})_i = (\Gamma_i - 1)E_i \gtrsim (\Gamma_f - 1)E_f + E_f = \Gamma_f E_f$. Given our estimates for E_i and E_f, we see that $\Gamma_i \gtrsim (\Gamma_i - 1)/\Gamma_f \gtrsim 70$. Such a large initial Lorentz factor is extremely unlikely for most jet geometries since the ejecta would be extremely Doppler de-boosted and intrinsically more luminous by orders of magnitude (in the manner of an off-axis gamma-ray burst). Therefore, we must conclude that our initial estimate of the initial internal energy, E_i, is at least two orders of magnitude too low (there is no clear way that E_f can have been overestimated), and that the majority of kinetic energy released is not well traced by early-time radio flaring.

Regardless of the powering mechanism, we may take $E_f \sim 10^{42}$ erg as a strong lower limit to the total energy supplied to the jet, and assume that the jet was launched over a phase of $\lesssim$6.7 h, the rise time of the optically thin flare during the state transition. From this, we derive a required energy supply rate to the launched ejection of 4×10^{37} erg s^{-1}, around 50% of the contemporaneous X-ray luminosity.

Conclusions

We present the following picture of the radio behaviour of J1820. A radio flare reveals the launch of relativistic transient ejecta as J1820 transitioned from the hard to soft X-ray state. We are able to track these ejecta to large separations from the black hole due to their high proper motions, and the sensitivity of MeerKAT to emission from larger angular scales. The initial fast decays (both the flare and region between MJD 58314 and MJD 58320; Extended Data Fig. 4, segment one) of the approaching component is caused by the evolution of the expanding ejecta. The subsequent re-brightening (MJD 58320 to MJD 58324) and slow decay (MJD 58324 onward; Extended Data Fig. 4, segment two) are the result of the ejecta continually interacting with the ISM and associated in situ particle acceleration as jet kinetic energy is lost. The physical size of the emission ~90 d after the ejection reveals a very large energy content in the ejecta, with an internal energy much larger than the internal energy estimated from the state transition radio flare. These observations and their interpretation present an unprecedented and comprehensive view of the life cycle of highly relativistic ejections from a stellar mass black hole over the first half a year after launch.

Methods

AMI-LA observations. We began an intensive monitoring campaign on J1820 with AMI-LA[44,45] 1.5 h after the Swift BAT triggered on the source, at 00:11:39 UT on 12 March 2018 (t_0 = MJD 58189.0709). The AMI-LA is robotically triggered by Swift BAT observations, and observes sources as soon as visibility constraints allow[19]. Between t_0 and MJD 58462.45, we observed J1820 with the AMI-LA for a total of 183 epochs. These data were all taken at a central frequency of 15.5 GHz across a 5 GHz bandwidth consisting of 4,096 channels, which we average down to 8 for imaging. Radio-frequency interference (RFI) flagging and bandpass and phase reference calibration were performed using a custom reduction pipeline[46]. Additional flagging and imaging was performed in the Common Astronomy Software Applications (CASA[47]) package. For imaging, we use natural weighting with a clean gain of 0.1. To measure the source flux density we use the CASA task IMFIT. The resolution of the AMI-LA (characteristic beam dimensions 40′ × 30″) when observing at the declination of J1820 mean that the source is unresolved in all epochs.

eMERLIN. We made observations of J1820 with the eMERLIN interferometer over the course of the 2018 outburst at 1.5 GHz and 5 GHz, for a total of 15 epochs. Data taken at 5 GHz (March and July 2018) was done so across a 512 MHz bandwidth, split into 4 spectral windows each of which consisted of 128 channels. Data taken at 1.5 GHz (October) also had a 512 MHz bandwidth, but instead was split into 8 spectral windows each consisting of 128 channels.

Data flagging and calibration were performed using version 0.9.24 of the eMERLIN CASA pipeline (https://web.archive.org/web/20190601000000*/https://github.com/e-merlin/eMERLIN_CASA_pipeline/) using standard calibration steps. We performed additional data flagging with AOFlagger[48]. For all of the observations, 3C286, OQ208 (QSO B1404+286) and J1813+0615 were used as the primary flux, bandpass and phase calibrators, respectively. Imaging was performed in CASA using standard procedures and natural weighting. While some observations had a bright core, allowing for the possibility of self-calibration, we opt to not perform additional calibration steps to preserve the absolute astrometry of our measurements. A summary of the eMERLIN observations, including participating antennas, is given in Supplementary Table 3.

MeerKAT. We first observed the location of J1820 with the MeerKAT radio interferometer at 17:46:40.5 UT on 28 September 2018 (MJD 58389.74) for a total of 15 min on source integration time. This observation was taken as part of the ThunderKAT large survey project[49]. Of the 64 antennas, 62 were used in the observation, with a maximum baseline of 7.698 km. Data were taken at a central frequency of 1.28 GHz across a 0.86 GHz bandwidth consisting of 4,096 channels each of width 209 kHz. We used J1939−6342 as the flux and bandpass calibrator. J1733−1304 was used as the complex gain calibrator, and was observed for 2 min before and after the source field. Additional observations were taken with identical instrument and calibrator setups (apart from the number of antennas). Data were flagged for RFI and other issues in both the CASA and AOFlagger software packages. In CASA, we flag the first and final 100 channels from the observing band, autocorrelations and zero amplitude visibilities. We then used AOFlagger to detect and remove RFI in the time and frequency domain. Flux scaling, bandpass calibration and complex gain calibration were all performed in CASA using standard procedures. After flagging and phase reference calibration, the data were averaged in time (8 s) and frequency (4 channels) for imaging. We used WSClean[50] to image the entire square degree field with uniform weighting, with the auto-masking threshold for deconvolution set to 4.5 times the (local) root mean square flux density. We use a clean gain of 0.1. We do not perform any self-calibration on the data, despite the ample flux density in the field, to preserve absolute astrometry. A summary of the MeerKAT observations is given in Supplementary Table 5.

Karl G. Jansky VLA. We observed J1820 with the VLA for a total of 10 epochs, beginning on 7 October, after the source had returned to the hard X-ray state. All observations were taken at C band and the VLA was either in D (its most compact) or C configuration. Data reduction was performed using standard procedures (for example, https://web.archive.org/web/20190601000000*/https://casaguides.nrao.edu/index.php/Main_Page).

VLBA. We observed J1820 for a single epoch on MJD 58306 with the VLBA. The source was observed for 1 h, reaching a root mean square noise of 140 μJy. In this observation, we detect both the approaching and receding jet component (the core was not detected as the source was in the soft state for this observation). Owing to the high proper motion, the source moves an angular distance greater than the synthesized beam of the array in 1 h, and as such is 'smeared' along the direction of motion. To measure the positions of the two components, we fit the main peak of the flux profile along the jet axis with a Gaussian, using the centroid as the position. To estimate the error on the position, we smooth the entire flux profile of each ejection along the jet axis using a Savitzky–Golay filter until the profile is Gaussian-like. We then fit this smoothed profile with a Gaussian, using the half-width at half-maximum as the error. These measurements are reported in Supplementary Table 1.

Radio positions. A critical part of our analysis relies on measuring the positions of the core and ejections from J1820 with a range of telescopes. For our observations with eMERLIN, MeerKAT and the VLA in C configuration, we fit the sources in the image plane using the CASA task IMFIT. For MeerKAT observations, we attempt to fit three point source (fixed beam major and minor axes and position angle) components, allowing the position and amplitude to vary. For MeerKAT observations where a three-component fit would not converge (early time observations when the receding jet had a small angular separation), we fit two components instead. We do not fix the core position in our MeerKAT analysis to the known position from our eMERLIN observations, so any systematic position errors will affect all components and be negated when calculating the separation. We used the same procedure for the VLA C configuration data. For eMERLIN observations, the components are substantially separated and as such can be boxed and fit individually using IMFIT. When fitting the ejection components, we do not fix the dimensions of the elliptical Gaussian used by IMFIT, as the ejection components are not point-like. We do fix the size of the component used to fit the (known to be compact) core. As core emission was not detected in all eMERLIN observations (due to core quenching in the soft state), we use the position measured from a bright observation on MJD 58201 to calculate the separation. We did not use the position errors reported by IMFIT for analysis, as we found these tended (especially for bright components) to be many times smaller than the synthesized beam. While the centroid of an elliptical Gaussian is known to an accuracy determined by the ratio of the synthesized beam dimensions to the signal-to-noise ratio of the Gaussian, this is only true to a certain accuracy level before absolute astrometric uncertainties begin to dominate. For example, it is recommended for the VLA (https://web.archive.org/web/20190601000000*/https://science.nrao.edu/facilities/vla/docs/manuals/oss/performance/positional-accuracy) that, unless special calibration steps are taken, positions are not reported to an accuracy of more than about 10% of the synthesized beam width. For all of our observations, we report position errors as A/σ, where A is the amplitude of the fit component and σ is the width of the synthesized beam at an angle connecting the fitted component with its corresponding ejection/core component, but never to an accuracy greater than 10% of this width (we confirm using check sources in the MeerKAT field that the position errors calculated as such are sensible). There are two exceptions to this. When, in our eMERLIN observations, only the core was detected, we simply report the IMFIT right ascension and declination errors, combined in quadrature. For eMERLIN observations when only an ejection component was detected, we use the observation taken on MJD 58201 for the purpose of finding the angle at which to calculate σ. For VLA observations taken when the array was in the more compact D configuration, the resolution was not good enough to fit sources in the image plane. For these observations, we performed fitting in the UV plane using the CASA task UVMULTIFIT[51], after building a sky model and subtracting background sources using the CASA task UVSUB. When fitting UV plane components, we fix the spectral index of the ejecta to be −0.7, but allow the core spectral index to vary as a free parameter. Components were all specified to be point sources. The results of the positions and flux densities measured from this analysis are presented in Supplementary Tables 1 and 2, respectively. The position errors from our VLBA observation are described in the Very Long Baseline Array subsection of the Methods. We do not correct the eMERLIN observations for the proper motion of the core as the change in separation caused by this motion ($\lesssim$3 mas) is $\lesssim$1% of the separation for all epochs, and is much less than the eMERLIN separation errors, which are $\geq$15 mas.

Swift X-ray Telescope. J1820 was observed at high brightness levels during a large fraction of its outburst phase with the Swift X-ray Telescope (XRT[52]). For this reason, most of the observations considered in this work have been taken using the XRT window-timing mode, which provides one-dimensional imaging with a 1.7 ms time resolution, and allows bright sources to be observed. Photon pile-up is known to induce distortion of the XRT's spectral response (see http://www.swift.ac.uk/analysis/xrt/pileup.php) and it starts to have non-negligible effects at a nominal count rate threshold of approximately 150 counts s^{-1}. Since J1820 was most of the time observed with count rates in the XRT much higher than this threshold, Swift/XRT data are often substantially affected by photon pile-up. Therefore, following the recommendation found in the Swift/XRT data reduction threads (http://www.swift.ac.uk/analysis/xrt/#abs), we extracted only grade 0 events from the raw data. This helps to mitigate the effects of pile-up in bright sources (http://www.swift.ac.uk/xrt_curves/cppdocs.php) and reduces the spectral distortion encountered in window-timing mode below 1.0 keV in case the energy spectrum is highly absorbed. Furthermore, we ignored data below 0.6 keV, as below this energy the energy spectra can be dominated by strong redistribution effects associated with the window-timing readout process, and by trailing charge released from deep charge traps in the CCD (charge-coupled device) on timescales comparable to the window-timing readout time, which results in additional (spurious) low-energy events.

To exclude the regions of the detector where pixels were pile-up saturated, we extracted events in circular regions centred at the source position, with variable inner radius and outer radius fixed to 20 pixels. We determined the final inner radius of the extraction region by varying it until the spectral shape was no longer changing as a function of the inner radius itself, and the count rate was lower than approximately 150 counts s^{-1}.

The spectral evolution of J1820 was generally slow (save for the times of the hard-to-soft-state transition, which was missed by Swift); hence, we extracted one spectrum per Swift/XRT observation. We obtained a total of 80 spectra for X-ray observations within 8 h of our AMI-LA observations, covering the entire duration of the outburst. As in this work we are interested in the source luminosity rather than its detailed spectral properties (to be presented in a future work), we fitted each spectrum between 0.6 and 10 keV using the XSPEC package[53] with a phenomenological model constituted by a simple power law model combined with a multicolour disk-blackbody (power law + disk in XSPEC), both modified by interstellar absorption (TBNEW_FEO). We then measured the source flux in the 1–10 keV energy band, which we converted the flux to luminosity using a distance from the source of 3.8 kpc.

Data availability

All radio maps used in our analysis are available from the corresponding author on reasonable request. The data used to create the radio–X-ray correlation (Fig. 1) are available in a Source Data file. The AMI-LA data of the radio flare shown in Extended Data Fig. 1 are available in a Source Data file. The authors declare that all other data supporting the findings of this study are available within the paper and its Supplementary Information.

Received: 30 July 2019; Accepted: 21 January 2020;
Published online: 2 March 2020

References

1. Fender, R. P., Belloni, T. M. & Gallo, E. Towards a unified model for black hole X-ray binary jets. *Mon. Not. R. Astron. Soc.* **355**, 1105–1118 (2004).
2. Corbel, S., Fender, R. P., Tomsick, J. A., Tzioumis, A. K. & Tingay, S. On the origin of radio emission in the X-ray states of XTE J1650−500 during the 2001–2002 outburst. *Astrophys. J.* **617**, 1272–1283 (2004).
3. Blandford, R. D. & Znajek, R. L. Electromagnetic extraction of energy from Kerr black holes. *Mon. Not. R. Astron. Soc.* **179**, 433–456 (1977).
4. Blandford, R. D. & Payne, D. G. Hydromagnetic flows from accretion disks and the production of radio jets. *Mon. Not. R. Astron. Soc.* **199**, 883–903 (1982).
5. Rees, M. J., Begelman, M. C., Blandford, R. D. & Phinney, E. S. Ion-supported tori and the origin of radio jets. *Nature* **295**, 17–21 (1982).
6. Stirling, A. M. et al. A relativistic jet from Cygnus X-1 in the low/hard X-ray state. *Mon. Not. R. Astron. Soc.* **327**, 1273–1278 (2001).
7. Dhawan, V., Mirabel, I. F. & Rodríguez, L. F. AU-scale synchrotron jets and superluminal ejecta in GRS 1915+105. *Astrophys. J.* **543**, 373–385 (2000).
8. Russell, D. M. et al. Testing the jet quenching paradigm with an ultradeep observation of a steadily soft state black hole. *Astrophys. J.* **739**, L19 (2011).
9. Coriat, M. et al. Radiatively efficient accreting black holes in the hard state: the case study of H1743−322. *Mon. Not. R. Astron. Soc.* **414**, 677–690 (2011).
10. Rushton, A. P. et al. Disc-jet quenching of the galactic black hole swift J1753.5−0127. *Mon. Not. R. Astron. Soc.* **463**, 628–634 (2016).
11. Russell, T. D. et al. Disk-jet coupling in the 2017/2018 outburst of the galactic black hole candidate X-ray binary MAXI J1535−571. *Astrophys. J.* **883**, 198 (2019).
12. Mirabel, I. F. & Rodríguez, L. F. A superluminal source in the galaxy. *Nature* **371**, 46–48 (1994).
13. Tucker, M. A. et al. ASASSN-18ey: the rise of a new black hole X-ray binary. *Astrophys. J.* **867**, L9 (2018).
14. Kawamuro, T. et al. MAXI/GSC detection of a probable new X-ray transient MAXI J1820+070. *The Astronomer's Telegram* 11399 (2018).
15. Uttley, P. et al. NICER observations of MAXI J1820+070 suggest a rapidly-brightening black hole X-ray binary in the hard state. *The Astronomer's Telegram* 11423 (2018).
16. Torres, M. A. P. et al. Dynamical confirmation of a black hole in MAXI J1820+070. *Astrophys. J.* **882**, L21 (2019).
17. Shappee, B. J. et al. The man behind the curtain: X-rays drive the UV through NIR variability in the 2013 active galactic nucleus outburst in NGC 2617. *Astrophys. J.* **788**, 48 (2014).
18. Kennea, J. A. et al. Swift detection of MAXI J1820+070. *The Astronomer's Telegram* 11403 (2018).
19. Staley, T. D. et al. Automated rapid follow-up of Swift gamma-ray burst alerts at 15 GHz with the AMI Large Array. *Mon. Not. R. Astron. Soc.* **428**, 3114–3120 (2013).
20. Gandhi, P., Rao, A., Johnson, M. A. C., Paice, J. A. & Maccarone, T. J. Gaia data release 2 distances and peculiar velocities for galactic black hole transients. *Mon. Not. R. Astron. Soc.* **485**, 2642–2655 (2019).
21. Shidatsu, M. et al. X-ray, optical, and near-infraredmonitoring of the new X-ray transient MAXI J1820+070 in the low/hard state. *Astrophys. J.* **868**, 54 (2018).
22. Shidatsu, M. et al. X-ray and optical monitoring of state transitions in MAXI J1820+070. *Astrophys. J.* **874**, 183 (2019).
23. Muñoz-Darias, T. et al. Hard-state accretion disk winds from black holes: the revealing case of MAXI J1820+070. *Astrophys. J.* **879**, L4 (2019).
24. Kajava, J. J. E. et al. X-ray dips and a complex UV/X-ray cross-correlation function in the black hole candidate MAXI J1820+070. *Mon. Not. R. Astron. Soc.* **488**, L18–L23 (2019).
25. Kara, E. et al. The corona contracts in a black-hole transient. *Nature* **565**, 198–201 (2019).
26. Fender, R. P., Homan, J. & Belloni, T. M. Jets from black hole X-ray binaries: testing, refining and extending empirical models for the coupling to X-rays. *Mon. Not. R. Astron. Soc.* **396**, 1370–1382 (2009).
27. Corbel, S. et al. The 'universal' radio/x-ray flux correlation: the case study of the black hole GX 339-4. *Mon. Not. R. Astron. Soc.* **428**, 2500–2515 (2013).
28. Brocksopp, C., Miller-Jones, J. C. A., Fender, R. P. & Stappers, B. W. A highly polarized radio jet during the 1998 outburst of the black hole transient XTE J1748−288. *Mon. Not. R. Astron. Soc.* **378**, 1111–1117 (2007).
29. Hjellming, R. M. & Rupen, M. P. Episodic ejection of relativistic jets by the X-ray transient GRO J1655-40. *Nature* **375**, 464–468 (1995).
30. Hannikainen, D. C. et al. Revisiting the relativistic ejection event in XTE J1550−564 during the 1998 outburst. *Mon. Not. R. Astron. Soc.* **397**, 569–576 (2009).
31. Atri, P. et al. A radio parallax to the black hole X-ray binary MAXI J1820+070. Preprint at https://arxiv.org/abs/1912.04525 (2019).
32. Fender, R. P. Uses and limitations of relativistic jet proper motions: lessons from galactic microquasars. *Mon. Not. R. Astron. Soc.* **340**, 1353–1358 (2003).
33. Longair, M. S. *High Energy Astrophysics* Ch. 16.4 (Cambridge Univ. Press, 2011).
34. Bright, J., Motta, S., Fender, R., Perrott, Y. & Titterington, D. AMI-LA 15.5 GHz observations of radio flaring from the black hole candidate MAXI J1820+070 in transition. *The Astronomer's Telegram* 11827 (2018).
35. van der Laan, H. A model for variable extragalactic radio sources. *Nature* **211**, 1131–1133 (1966).
36. Tetarenko, A. J. et al. Extreme jet ejections from the black hole X-ray binary V404 Cygni. *Mon. Not. R. Astron. Soc.* **469**, 3141–3162 (2017).
37. Fender, R. & Bright, J. Synchrotron self-absorption and the minimum energy of optically thick radio flares from stellar mass black holes. *Mon. Not. R. Astron. Soc.* **489**, 4836–4846 (2019).
38. Hannikainen, D. et al. XTE J1550-564: a superluminal ejection during the september 1998 outburst. *Astrophys. Space Sci. Suppl.* **276**, 45–48 (2001).
39. Corbel, S. et al. Large-scale, decelerating, relativistic X-ray jets from themicroquasar XTE J1550−564. *Science* **298**, 196–199 (2002).
40. Tomsick, J. A. et al. X-ray jet emission from the black hole X-ray binary XTE J1550−564 with Chandra in 2000. *Astrophys. J.* **582**, 933–944 (2003).
41. Migliori, G. et al. Evolving morphology of the large-scale relativistic jets from XTE J1550−564. *Mon. Not. R. Astron. Soc.* **472**, 141–165 (2017).
42. Corbel, S. et al. Discovery of X-ray jets in the microquasar H1743−322. *Astrophys. J.* **632**, 504–513 (2005).
43. Wang, X. Y., Dai, Z. G. & Lu, T. External shock model for the large-scale, relativistic X-ray jets from the microquasar XTE J1550−564. *Astrophys. J.* **592**, 347–353 (2003).
44. Zwart, J. T. L. et al. The Arcminute Microkelvin Imager. *Mon. Not. R. Astron. Soc.* **391**, 1545–1558 (2008).
45. Hickish, J. et al. A digital correlator upgrade for the Arcminute Microkelvin Imager. *Mon. Not. R. Astron. Soc.* **475**, 5677–5687 (2018).

46. Perrott, Y. C. et al. AMI galactic plane survey at 16 GHz — I. Observing, mapping and source extraction. *Mon. Not. R. Astron. Soc.* **429**, 3330–3340 (2013).
47. McMullin, J. P., Waters, B., Schiebel, D., Young, W. & Golap, K. CASA architecture and applications. In *Astronomical Data Analysis Software and Systems XVI* ASP Conference Series Vol. 376 (eds Shaw, R. A. et al.) 127–130 (ASP, 2007).
48. Offringa, A. R., van de Gronde, J. J. & Roerdink, J. B. T. M. A morphological algorithm for improving radio-frequency interference detection. *Astron. Astrophys.* **539**, A95 (2012).
49. Fender, R. et al. ThunderKAT: the MeerKAT large survey project for image-plane radio transients. Preprint at https://arxiv.org/abs/1711.04132 (2017).
50. Offringa, A. R. et al. WSCLEAN: an implementation of a fast, generic wide-field imager for radio astronomy. *Mon. Not. R. Astron. Soc.* **444**, 606–619 (2014).
51. Martí-Vidal, I., Vlemmings, W. H. T., Muller, S. & Casey, S. UVMULTIFIT: a versatile tool for fitting astronomical radio interferometric data. *Astron. Astrophys.* **563**, A136 (2014).
52. Gehrels, N. et al. The Swift gamma-ray burst mission. *Astrophys. J.* **611**, 1005–1020 (2004).
53. Arnaud, K. A. XSPEC: the first ten years. In *Astronomical Data Analysis Software and Systems V* ASP Conference Series Vol. 101 (eds Jacoby, G. H. & Barnes, J.) 17–20 (ASP, 1996).
54. Motta, S. E., Casella, P. & Fender, R. P. Radio-loudness in black hole transients: evidence for an inclination effect. *Mon. Not. R. Astron. Soc.* **478**, 5159–5173 (2018).
55. Drappeau, S. et al. Dark jets in the soft X-ray state of black hole binaries? *Mon. Not. R. Astron. Soc.* **466**, 4272–4278 (2017).

Acknowledgements

J.S.B. acknowledges the support of a Science and Technologies Facilities Council Studentship. E.T. acknowledges financial support from the UnivEarthS Labex programme of Sorbonne Paris Cité (ANR-10-LABX-0023 and ANR-11-IDEX-0005-02). D.A.H.B. acknowledges support by the National Research Foundation. P.A.W. acknowledges support from the NRF and UCT. J.C.A.M.-J. is the recipient of an Australian Research Council Future Fellowship (FT140101082), funded by the Australian government. A.H. acknowledges that this research was supported by a grant from the GIF, the German-Israeli Foundation for Scientific Research and Development. I.H. and D.R.A.W. acknowledge support from the Oxford Hintze Centre for Astrophysical Surveys, which is funded through generous support from the Hintze Family Charitable Foundation. J.M. acknowledges financial support from the State Agency for Research of the Spanish MCIU through the 'Center of Excellence Severo Ochoa' award to the Instituto de Astrofísica de Andalucía (SEV-2017-0709) and from the grant RTI2018-096228-B-C31 (MICIU/FEDER, EU).

The MeerKAT telescope is operated by the South African Radio Astronomy Observatory, which is a facility of the National Research Foundation, an agency of the Department of Science and Technology. We thank the staff of the Mullard Radio Astronomy Observatory for their invaluable assistance in the commissioning, maintenance and operation of AMI, which is supported by the universities of Cambridge and Oxford. We acknowledge support from the European Research Council under grant ERC-2012-StG-307215 LODESTONE. We thank the Swift team for performing observations promptly on short notice. The National Radio Astronomy Observatory is a facility of the National Science Foundation operated under cooperative agreement by Associated Universities, Inc. e-MERLIN is a National Facility operated by the University of Manchester at Jodrell Bank Observatory on behalf of STFC. We acknowledge the use of the Inter-University Institute for Data Intensive Astronomy (IDIA) data-intensive research cloud for data processing. IDIA is a South African university partnership involving the University of Cape Town, the University of Pretoria and the University of the Western Cape. We thank the International Space Science Institute in Bern, Switzerland for support and hospitality for the team meeting 'Looking at the disc–jet coupling from different angles: inclination dependence of black-hole accretion observables'.

Author contributions

J.S.B. led interpretation of results, wrote a substantial portion of the manuscript, and performed the reduction of the MeerKAT and AMI-LA data. R.P.F. contributed to the interpretation of results and wrote a substantial portion of the manuscript. S.E.M. contributed to the interpretation of results and performed the reduction of the Swift and MAXI X-ray data. J.C.A.M.-J. contributed to the interpretation of results. D.R.A.W., J.M. and R.B. performed the reduction of the eMERLIN data. R.M.P. and J.C.A.M.-J. performed the reduction of the VLA data. J.C.A.M.-J. performed the reduction of the VLBA data. I.H. and E.T. assisted with the reduction of the MeerKAT observational data. D.T., D.A.G., G.R.S., A.J.T., T.D.R. and D.A.H.B. provided useful comments on the manuscript. S.C., J.H., E.G., P.A.W., R.P.A., P.J.G., A.H., A.J.v.d.H., E.G.K., V.A.M., A.R. and R.A.M.J.W. provided useful comments on the manuscript, and were instrumental in the organization and implementation of the ThunderKAT large survey project.

Competing interests

The authors declare no competing interests.

Additional information

Extended data is available for this paper at https://doi.org/10.1038/s41550-020-1023-5.

Supplementary information is available for this paper at https://doi.org/10.1038/s41550-020-1023-5.

Correspondence and requests for materials should be addressed to J.S.B.

Peer review information *Nature Astronomy* thanks Michael McCollough and the other, anonymous, reviewer(s) for their contribution to the peer review of this work.

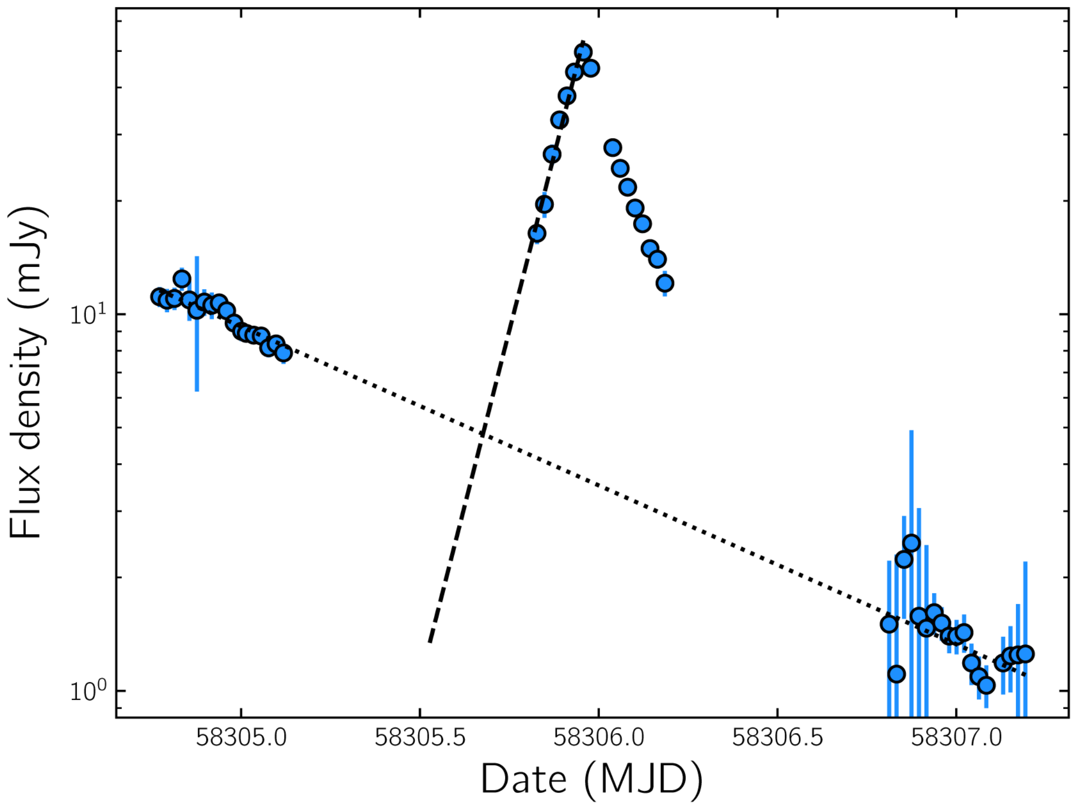

Extended Data Fig. 1 | AMI-LA observations of a state transition radio flare from J1820. AMI-LA observations of a radio flare which occurred as J1820 transitioned from the hard to soft X-ray state. The blue data points correspond to 30 min of (u,v) amplitudes averaged over all baselines and frequencies. The errors on individual points include a statistical error (calculated from the standard deviation of data within the 30 min bin) and a 5% calibration uncertainty, combined in quadrature. Dotted and dashed lines show exponential fits to the core quenching and the rise of the flare, respectively. We use these to estimate the rise time of the flare, which we take as the time between the intercept of these fits and the peak data point of the flare, as well as its start date. Error bars on data points indicate one sigma uncertainties.

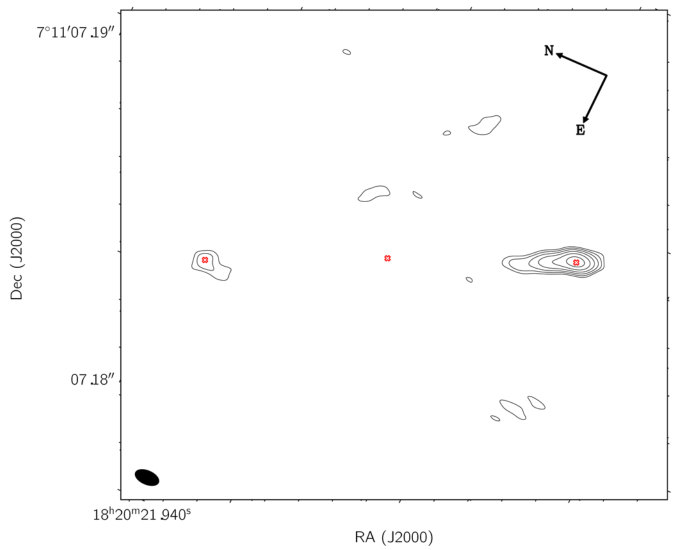

Extended Data Fig. 2 | A VLBA observation of J1820 from MJD 58306.22. Contours mark 140 μJy × $(\sqrt{2})^n$ for $n = 3, 4, 5, 6, 7, 8, 9$. We mark the position of the core (central red cross; inferred from previous hard state observations) and the measured positions of the approaching (red cross to the right of the core) and receding (red cross to the left of the core) jet from the image. These are given in Supplementary Table 1. The black ellipse in the bottom left corner shows the synthesised beam with a major and minor axis of 0.0009′ and 0.0005′, respectively.

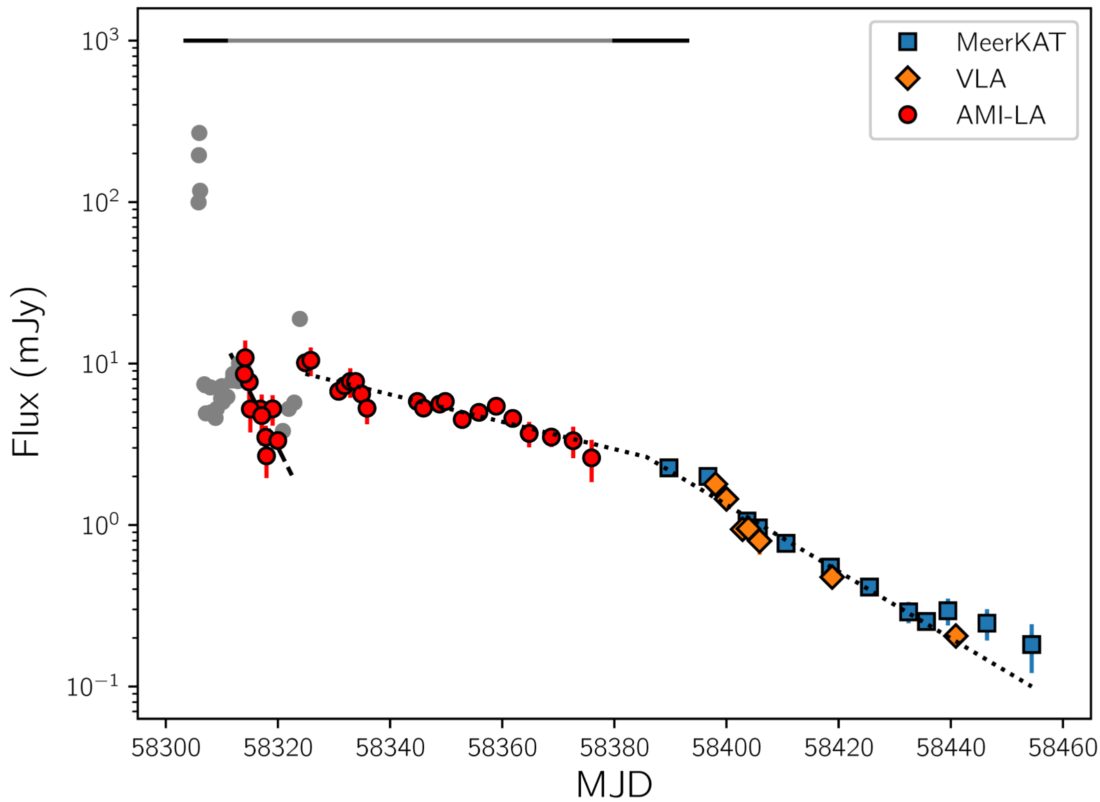

Extended Data Fig. 3 | The radio flux density from the approaching radio ejecta over a 150 d period, starting near our inferred ejection. As with Fig. 4, with the eMERLIN and VLBA data removed. We fit sections of the light curve with exponential decay functions of the form $F_\nu = Ae^{-\Delta t/\tau}$. Data shaded grey are not included in the fitting. The first light curve segment (fast decaying AMI-LA data; MJD 58314 to 58320), is well described ($\chi^2_\nu = 1.21$) by a decay with a characteristic time scale of 6 ± 1d (dashed line). We opt to fit the apparently slower decay (MJD 58324 onward) with a broken exponential function (dotted line). The best fit decay rates are 51 ± 6 d and 21.0 ± 0.9 d, with the break occurring at MJD 58386 ± 4 ($\chi^2_\nu = 1.59$). Error bars on data points indicate one sigma uncertainties.

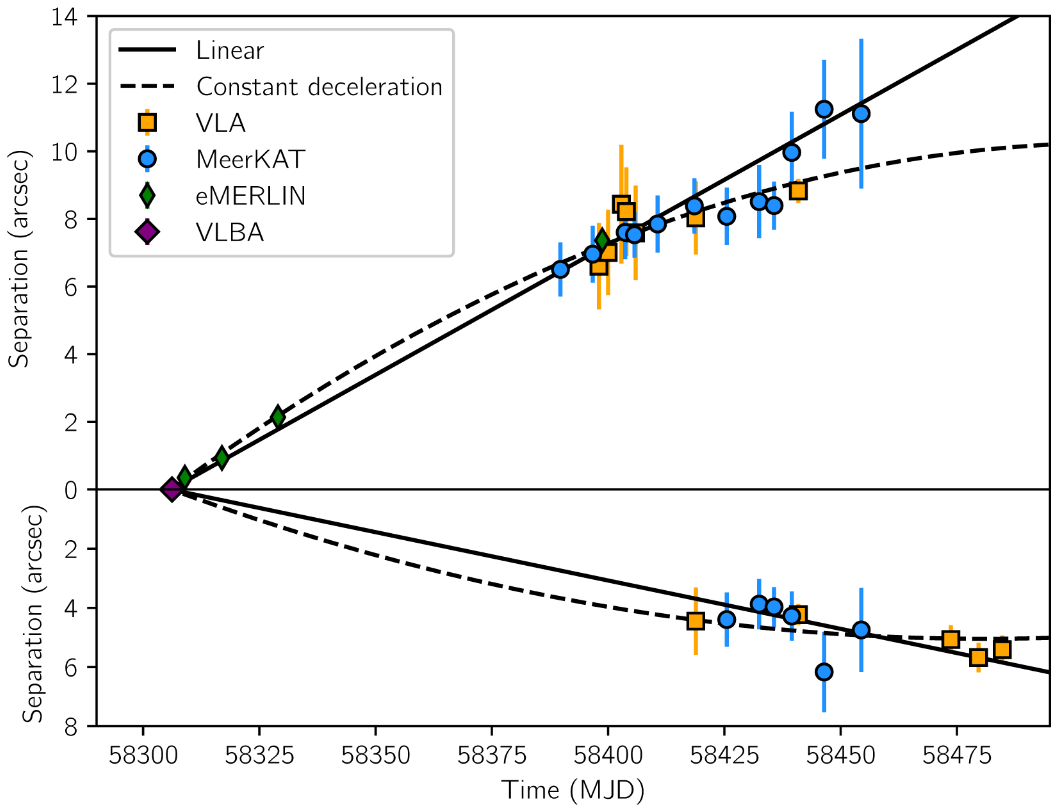

Extended Data Fig. 4 | The angular separation evolution of the approaching and receding jet components. The angular separation of the approaching (top panel) and receding (bottom panel) ejections from J1820 with time. We jointly fit both the approaching and receding jet motion with two models. Firstly we assume that both components propagate with ballistic motion and were launched simultaneously. For this case we find $\mu_{app} = 77 \pm 1$ mas d^{-1}, $\mu_{rec} = 33 \pm 1$ mas d^{-1} and $t_{launch} = 58305.89 \pm 0.02$ ($\Delta t = 0.21 \pm 0.02$) (quantities correspond to the approaching jet velocity, the receding jet velocity and the launch time, respectively). The best fit for this model are shown by the solid black lines in the top and bottom panel. Assuming now as above, but allowing for the proper motion of each component to undergo constant deceleration, we find $\mu_{app,0} = 101 \pm 3$ mas d^{-1}, $\mu_{rec,0} = 58 \pm 6$ mas d^{-1}, $t_{launch} = 58306.03 \pm 0.02$ ($\Delta t = 0.35 \pm 0.02$), $\dot{\mu}_{app} = -0.49 \pm 0.06$ mas d^{-2} and $\dot{\mu}_{rec} = -0.33 \pm 0.07$ mas d^{-2} (quantities correspond to the initial approaching jet velocity, the initial receding jet velocity, the launch time, the deceleration of the approaching jet and the deceleration of the receding jet, respectively). Error bars on data points indicate one sigma uncertainties.